EXPERIMENTAL AND NUMERICAL BEHAVIOUR OF WELDED STAINLESS STEEL BEAM-TO-COLUMN CONNECTIONS SUBJECTED TO CYCLIC LOADING

Xiaojun Wei [a], Hao Zhou [a,*], George S. Kamaris [b], Michaela Gkantou [b], Feiyu Yun [a], Xianglong Zuo [a], Xinran Guo [a], Shafayat Bin Ali [b, c]

[a] School of Civil Engineering, Central South University, Changsha 410075, PRC

[b] School of Civil Engineering and Built Environment, Liverpool John Moores University, United Kingdom

[c] Institute of Earthquake Engineering Research, Chittagong University of Engineering & Technology, Chattogram-4349, Bangladesh

*Corresponding author: hao.zhou@csu.edu.cn

This paper presents an experimental and numerical programme on six welded stainless steel beam-to-column connections subjected to cyclic loading. The test specimens were designed in accordance with Eurocodes and comprised an I-section beam made from 316L stainless steel welded to an I-section column made from 304L stainless steel. Each specimen was subjected to a quasi-static cyclic loading protocol and the load-displacement curves are monitored and reported. The results are analysed in terms of failure characteristics, skeleton curve, strain distribution and energy dissipation. Typical failure modes are combined global flexural and torsional buckling and localized web and flange buckling of the beams. The slope of skeleton curve in the hardening region and the energy dissipation capacity appeared to reduce with the section size. Numerical models capable of successfully replicating the experimentally observed response were developed. The load-displacement behaviour and the failure pattern were compared to the experimental ones, showing a good validation. Overall, it has been demonstrated that good hysteretic performance has been achieved for the welded stainless steel beam-to-column connections.

KEYWORDS

Welded stainless steel, beam-to-column connection, cyclic loading, finite element modelling, hysteresis behaviour

1. Introduction

Stainless steel is a structural material that has gained popularity in construction industry due to its desirable features, such as excellent durability, corrosion resistance and aesthetic appearance [1-4]. These characteristics have made stainless steel particularly attractive for offshore engineering applications in highly corrosive environments [5, 6]. Moreover, the superior mechanical properties of stainless steel, i.e., high strength, stiffness and ductility, have recently led to an increase of its use in a wide range of structural applications, which include towers, buildings, domes and bridges [1-6]. Finally, the nonlinear stress-strain behaviour and cyclic hardening exhibited by stainless steel are also ideal properties for seismic design of structures and thus provide a potential of its use in earthquake prone regions [4-7].

For the abovementioned reasons, research has been performed on the structural response of stainless steel members under monotonic and cyclic loading conditions. Extensive experimental and numerical studies have been reported on the static loading carrying capacity of stainless steel columns [3, 8-12], beams [8, 13-17] and beam-columns [18-24]. However, literature on the hysteretic behaviour of stainless steel is very limited and is mainly focused on the material level [4, 6, 25-27]. Significantly fewer studies investigate the behaviour of stainless steel members, i.e., braces [28, 29], columns [30, 31], beams [7, 32], and beam-columns [33-36], subjected to cyclic loading.

Connections are key elements in metal structures, as they are responsible for force and moment transfer between the connected members and thus can significantly affect the strength, stiffness, ductility and robustness of the whole structure[37, 38]. Stainless steels exhibit strongly nonlinear material behaviour with high ductility and pronounced strain-hardening. These characteristics which differ from those of carbon steel are expected to affect the performance of connections and thus warrant separate investigations. Nevertheless, the response of stainless steel connections has received relatively limited attention to date.

A few studies have been reported on the behaviour of stainless steel connections subjected to static loading. Bouchaïr et al. [39] examined the behaviour of bolted austenitic stainless steel connections and analysed the effects of material strain hardening on failure patterns, concluding that a ductile failure can be expected when stainless steel is used. Hasan et al. [40, 41] studied top-seat angle bolted connections produced from austenitic stainless steel and proposed an analytical model to predict the moment-rotation behaviour of the connection. Elflah et al. [42-44] conducted an experimental and numerical programme to investigate the performance of beam-to-column joints, concluding that the specifications of Eurocode 3 [45] are overly conservative in terms of strength and inaccurate in terms of stiffness. Yuan et al. [46] studied austenitic and duplex stainless steel T-stubs under monotonic loading and found that the existing design methods provide generally conservative predictions. A calculation method for determination of the initial stiffness and plastic resistance of stainless steel T-stubs was subsequently proposed by Yuan et al. [47]. Contrary to austenitic and duplex grades, existing design rules were found to offer good prediction of the moment resistance in case of ferritic stainless steels, according to Yapici et al. [46, 48]. During these investigations, the authors examined experimentally and numerically the performance of stainless steels T-stubs, considering various geometric configurations. In these studies, both the flexural and the membrane component of the load transfer mechanism were discussed, whilst the effect of material anisotropy on the plastic and ultimate resistance of bolted T-stubs for different stainless steel grades was analysed.

Even more limited is the research on stainless steel connections under cyclic loading conditions. Bu et al. [5] studied bolted stiffened extended end-plate connections under seismic loading, concluding that European design rules underestimate the plastic moment capacity of the connections. They also recommended additional surface treatment for stainless steel connections to guarantee friction grip. Experimental tests on stainless steel T-stubs were carried out by Yuan et al. [49], who found pronounced strain-hardening characteristics and more favourable hysteretic performance compared to carbon steel counterparts. Finally, Gao et al. [50, 51] conducted experiments on double extended end-plate beam-to-column joints subject to cyclic loading and found that the ductility demands provided by seismic design standards were exceeded.

It has been demonstrated by different numerical studies that the use of stainless steel members in earthquake-resistant structures can significantly improve their performance compared to their carbon steel counterparts and can be beneficial in terms of plastic deformations and energy dissipation capacity [52, 53]. These results show the potential application of stainless steel in seismic design of structures. However, the models used in these studies are not accurate, because they are not calibrated based on experimental data of the hysteretic behaviour of stainless steel beam-to-column connections, since such data are very limited. Therefore, experimental work on the investigation of the cyclic response of stainless steel beam-to-column connections is essential for a better understanding of the seismic behaviour of stainless steel structures. In addition, it can be seen from the above that most of the existing studies on stainless steel beam-to-column connections subject to cyclic loading focus on the behaviour of bolted connections. The hysteretic behaviour of welded stainless steel beam-to-column connections has never been investigated even though this type of connections is very common in seismic design. Aiming to bridge this knowledge gap, the present paper investigates the hysteretic performance of six welded beam-to-column connections under quasi-static cyclic loading conditions. To the best of the authors' knowledge, this is the first study to focus on welded stainless steel beam-to-column connections and the reported test data are very important as they contribute to the currently limited stainless steel connections data pool. To this end, the experimental programme is presented in Section 2 and a finite element (FE) model is developed in section 3. The experimental and numerical results analysed and discussed in Section 4 and the main conclusions are summarised in Section 5.

2. Experimental programme

2.1 Test specimens design

To investigate the hysteretic behaviour of the welded stainless steel beam-to-column connections under cyclic loading, a total of 6 specimens were designed and tested. The prototype building of Fig. 1(a) [54] was used in this study. The specimens were extracted from the exterior moment-resisting frame (MRF) shown in Fig. 1(b) of the prototype building. More specifically, the exterior joints of the second, third and fourth storeys of the prototype MRF were used as case studies for the experimental tests (Fig. 1(b)). The experiments were performed on three 2：5-scale models (i.e., scaling factor $\lambda = 0.4$; Tests 1-3) and three 2.25:5-scale models (i.e., scaling factor $\lambda = 0.45$; Tests 4-6) of the prototype joints. Two values of λ were utilised to investigate the size effect on the behaviour of the connections and to increase the number of the experimental data. The scaling factors values were also chosen considering the availability of the stainless steel material in the Chinese market and the capabilities of the lab. The specimens were designed based on the dimensions of the scaled joints in accordance with Eurocode 3 [55] and Eurocode 8 [56]. The scaling of the models was done assuming material scaling identity and the similitude scaling factors between the prototype joints and the test specimens are shown in Table 1. The beams and columns used in the tests were fabricated from stainless steel plates, which were welded to form an I-shape cross-section, which had similar dimensions to the prototype beams and columns, respectively, scaled by λ. A typical beam-to-column specimen is shown in Fig. 2(a). The specimen consists of a beam made of 316L stainless steel (vertical member) and a column made of 304L stainless steel (horizontal member). The length of the beam is equal to L1 and that of the column is equal to L2. Detailed dimensions of the specimens are presented in Table 2 and the notation used in this table is shown in Fig. 2(b). While manufacturing the specimens, the stainless steel plates were argon arc welded using ER304L electrodes supplied by AoBeiGao. The leg length of the fillet weld (both sides) of the beam is 7mm, while the size of the welding of the column is 10mm. The chamfer size at the beam-to-column intersection position was 15mm (Fig. 2a).

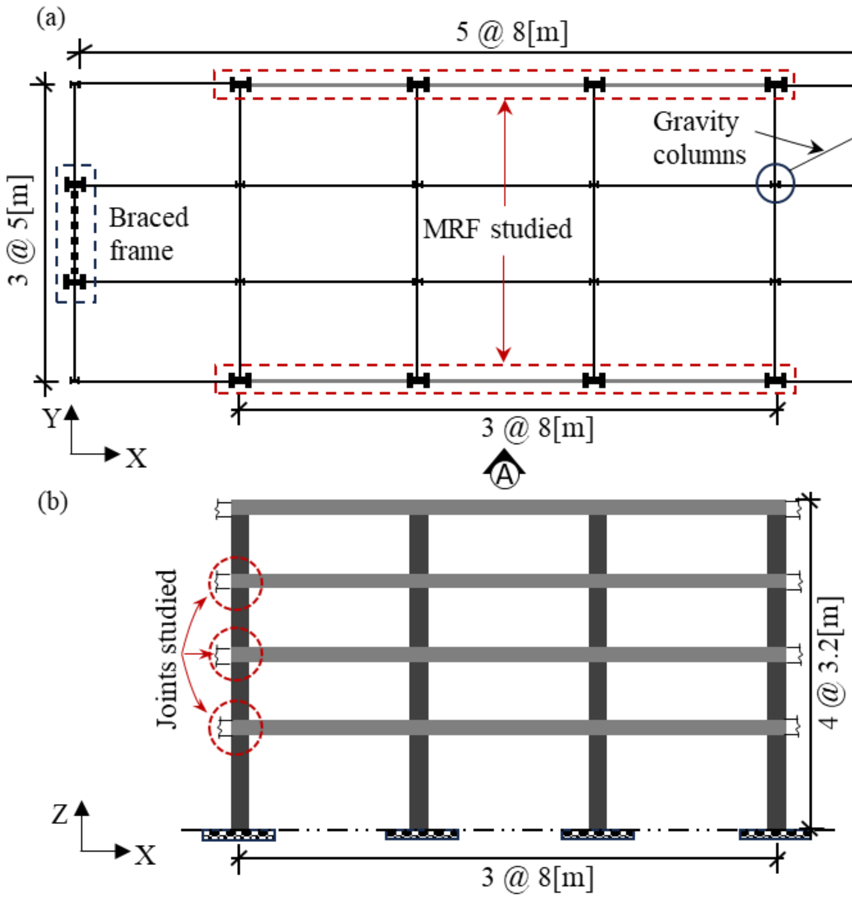

Fig. 1. Prototype building: (a) Plan view; and (b) Elevation A.

Table 1 Similitude scaling factors.

Scaling quantity	Units	Dimensional scale requirement	Scaling factor ($\lambda = 0.4$)	Scaling factor ($\lambda = 0.45$)
Length or displacement	L	λ	0.4	0.45
Area	L^2	λ^2	0.16	0.203
Section modulus	L^3	λ^3	0.064	0.091
Moment of inertia	L^4	λ^4	0.026	0.041
Stress	S	1	1	1
Force	$F = S \times L^2$	λ^2	0.16	0.203
Moment	$F \times L = S \times L^3$	λ^3	0.064	0.091

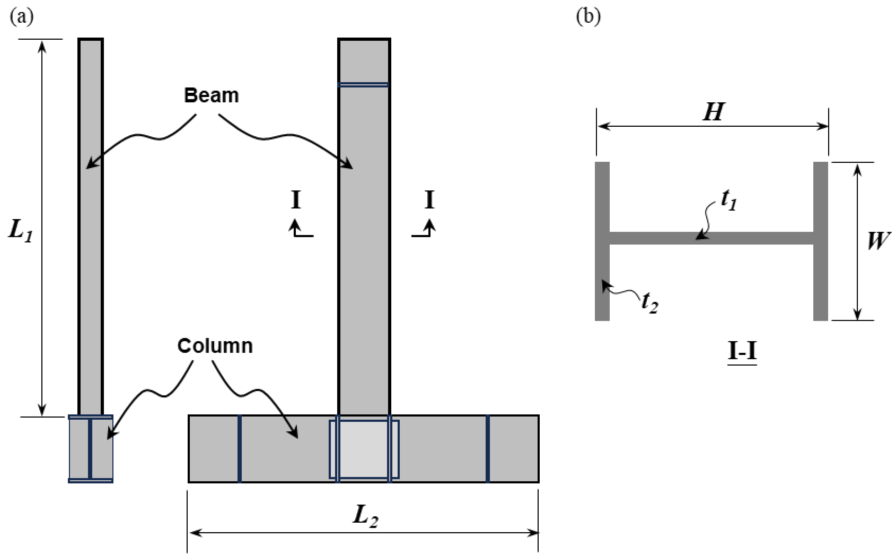

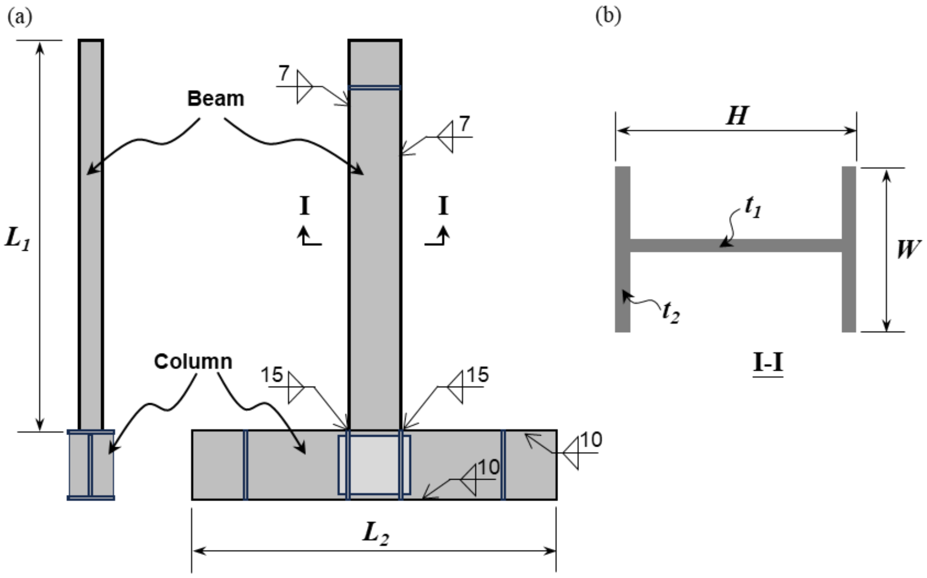

Fig. 2. (a) Beam-to-column specimen; and (b) notation of the cross-section.

Table 2 Specimen dimensions and test configuration (in [mm]).

Test	Beam Geometry					Column Geometry					Loading and Side Constraint Position		
	H	W	t_1	t_2	L_1	H	W	t_1	t_2	L_2	l_1	l_2	l_3
Test-1	240	88	6	8	1677	260	120	6	12	1280	513	1088	1463
Test-2	220	84	5	7.5	1677	260	120	6	12	1280	513	1088	1463
Test-3	200	80	5	6	1677	260	120	6	12	1280	513	1088	1463
Test-4	270	100	7.5	8	1861	292	135	8	14	1280	513	1150	1647
Test-5	250	95	5	8	1861	292	135	8	14	1280	513	1150	1647
Test-6	225	90	5	7.5	1861	292	135	8	14	1280	NA	NA	1647

2.2 Material properties of stainless steel

In this study, 316L and 304L stainless steel grades were used to fabricate the beam-to-column specimen. Therefore, uniaxial tensile tests were carried out to determine mechanical properties of stainless steel according to ISO 6892-1: 2009 [57]. For each steel grade, a total of 6 coupons (Fig. 3(a)) were tested using a universal testing machine. During the test, the strain was recorded by two strain gauges attached at both sides of the coupons, while the corresponding force was obtained by the testing machine.

Fig. 3(b) illustrates the engineering stress-strain relations for both 316L and 304L. Both 316L and 304L exhibit significant ductility and strain-hardening behaviour. It is evident that the material response of 316L and 304L is similar. The material model proposed by Arrayago et al. [58] was applied to model the tensile behaviour of the 316L and 304L under uniaxial tensile loading. The average modulus of elasticity of the stainless steel used in this study was determined as 188.6 [GPa].

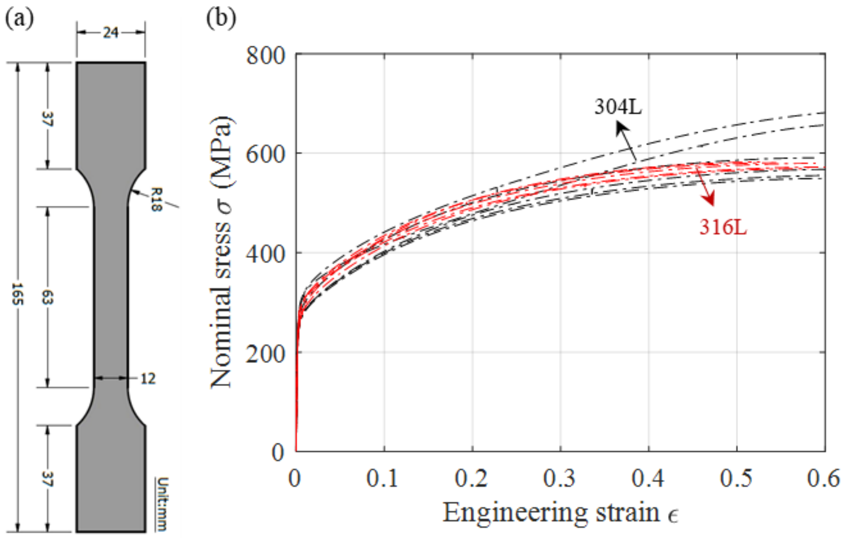

Fig. 3. Stainless steel material tests: (a) typical coupon geometry; and (b) stress-strain curves.

2.3 Test set-up and instrumentation

The stainless steel beam-to-column specimens of this study were tested employing the test set-up shown in Fig. 4. The load was applied perpendicular to the beam by a hydraulic actuator positioned at distance l_3 from the inner face of the column, as shown in Fig. 4 (loading point). The actuator is attached to the specimen by 4 threaded bars. To increase the local stiffness of the beam at the loading point, an internal web stiffener was welded to the beam at this point. The column of the specimen was bolted to the test rig, which comprised a stiff steel member, two stiff steel blocks and two steel plates. The stiff steel member was strengthened by internal web stiffeners to avoid any localised failure. The stiff steel blocks were welded to the stiff steel member and placed on each side of the column to restrain its horizontal movement. The steel plates were welded on the stiff steel member and bolted on the strong floor. Such test set-up is justified as this study mainly investigates the welding performance and deformation of the beam under cyclic loading. Therefore, the column was fixed by the bolts such that the effect of column deformation on the connection behaviour can be avoided.

To prevent out-of-plane movement of the beam during loading, bracing was installed on both sides of the beam-to-column specimen. The bracing was attached to the beam through rectangular hollow sections (RHSs) which were adjusted to restrain the out-of-plane deformation. Moreover, lubricating oil was pasted on the RHSs to reduce the friction between the beam and the bracing. The distance between the inner face of the column to the centre of the lower RHS (l_1), to the upper

RHS (l_2) and to the loading point (l_3), are shown in Fig. 4 and reported in Table 2. Note that l_2 is lower for Tests 1-3 compared to Tests 4-6, as in Tests 1-3, as one pair of RHS beams was removed in the latter to avoid contact between the actuator and the bracing.

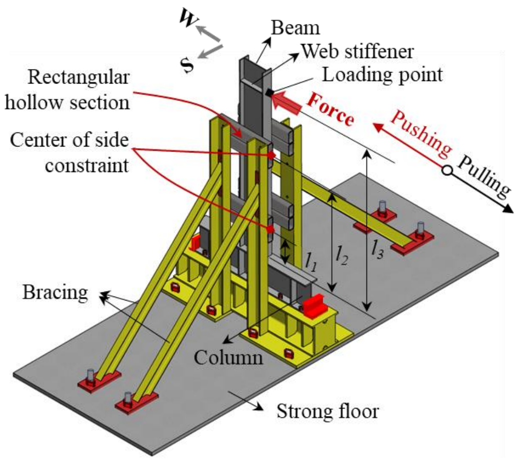

Fig.4. Test set-up.

Fig. 5 shows the instrumentation applied in each specimen. A pull string displacement senor was used at the loading point to record the horizontal displacement of the beam. In addition, two linearly varying displacement transducers (LVDTs), one 300 [mm] from the top of the column (LVDT-1) and one on the top flange of the column (LVDT-2) were attached to the specimens. The measurement of LVDT-1 was used to calculate the rotation angle of the beam during loading, and LVDT-2 was used to monitor the possible rigid-body movement of the specimen. A total of 24 stain gauges were used to measure the strain distribution parallel to the beam's axis at critical locations. In particular, the FE1-3 and FW1-3 strain gauges were attached on the east and west flange of the beam, respectively, as shown in Fig. 5(a). Moreover, 18 strain gauges were mounted on both sides of the web, namely WN1-9 and WS1-9 in the north and south side of the web, respectively (Fig. 5(a)). Note that both WN and WS series are named from the left to the right while facing the specimen, i.e., WN1 and WS3 are at the same planar position of the web. The strain gauges WN2,5,8 and WS2,5,8 are positioned at the centreline of the beam. All measurements were recorded at a frequency of 5 Hz.

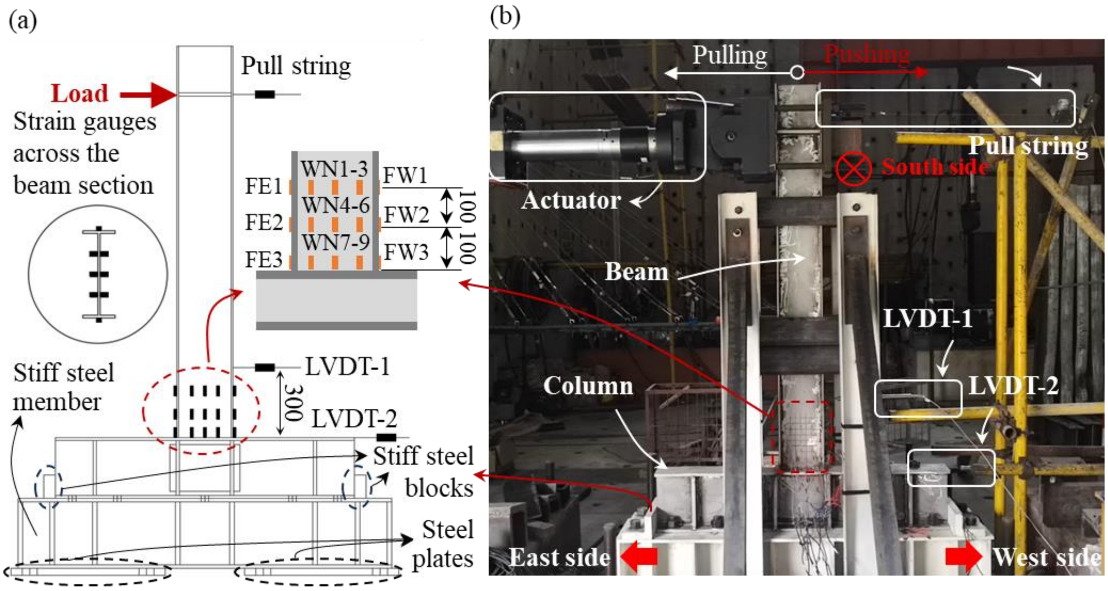

Fig. 5. Instrumentation: (a) schematic diagram (dimensions in [mm]); and (b) photograph of the test set-up and applied instrumentation.

2.4 Loading protocol

To investigate the cyclic behaviour of the welded stainless steel beam-to-column connections, the American Institute of Steel Construction [59] loading protocol was applied to each specimen (Fig. 6 and Table 3). This protocol consists of 34 loading cycles of imposed horizontal displacement of increasing amplitude applied in a quasi-static fashion. Regardless of the size and height of the specimen, the loading was applied based on the interstory drift angle, θ, calculated by dividing the horizontal displacement by the beams' height. As such, the flexural behaviour of the connections can be fairly compared. Thus, the loading protocol comprised three initial sets of six cycles at θ equal to 0.00375, 0.005, 0.0075 rad, four subsequent cycles at θ equal to 0.01 rad, and six sets of two cycles at θ equal to 0.015, 0.02, 0.03, 0.04, 0.05 and 0.06 rad. In the notation "LC*x*-*y*Ps/Pl" of Fig. 6, "LC" represents the cyclic loading type distinct by the interstory drift angle. "*x*" and "*y*" represent the x^{th} loading cycle type and y^{th} loading cycle in this load condition, respectively. Besides, Ps and Pl represent pushing and pulling load conditions in a full loading cycle, respectively. Specifically, pushing load represents the load direction at which the beam is moving away from the loading actuator, whereas pulling load represents the load direction at which the beam is moving towards the loading actuator. The displacement in pulling load direction is negative and in pushing load direction is positive. Finally, the load was applied through displacement-control at a rate of approximately 21 mm/min.

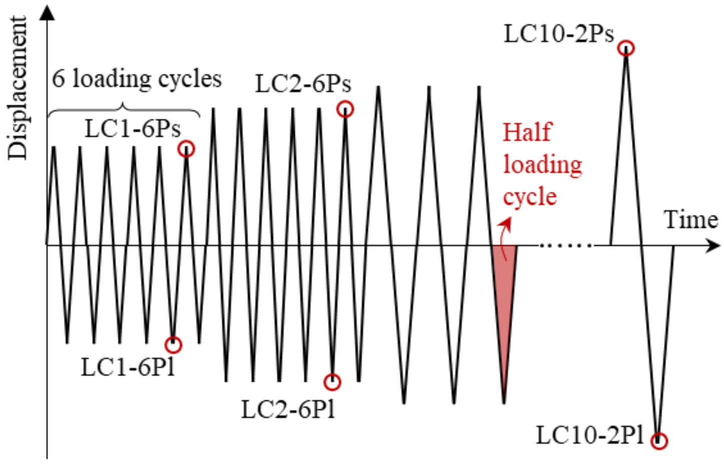

Fig. 6. Loading protocol.

Table 3 Loading procedure.

Cycle type	No of cycles	Interstory drift angle, θ (rad)	Horizontal displacement [mm]	
			Tests 1, 2 and 3	Tests 4, 5 and 6
1	6	0.00375	5.51	6.20
2	6	0.005	7.35	8.27
3	6	0.0075	11.03	12.41
4	4	0.01	14.70	16.54
5	2	0.015	22.05	24.81
6	2	0.02	29.40	33.08
7	2	0.03	44.10	49.62
8	2	0.04	58.80	66.16
9	2	0.05	73.50	82.70
10	2	0.06	88.20	99.24

3. Finite element modelling

In order to further investigate the cyclic behaviour of the stainless steel beam-to-column connections, a detailed 3D FE model was developed (Fig. 7) in Abaqus [60]. In the finite element model, all steel plates were simulated using shell elements (S4R) to enhance the computational efficiency, while accurately capturing the response of stainless steel I-sections [61, 62]. Tie constraints were used to connect the web and flanges of the beam and column to simulate the welding. Regarding the boundary conditions, the bottom surface of the column was fixed. To simulate the constraint provided by the side bracings, the translational degree of freedom in the x-direction of the beam at the bracing positions was constrained, as shown in Fig. 7(a). The load was applied through a reference point at the loading point which was tied to the contacting surface between the actuator and the beam. The static-standard solver was employed to solve the nonlinear problem.

Material response of the specimens was simulated by the von Mises yield criterion, based on the true stress-strain curves obtained during tensile tests (see Fig. 3(b)). In line with past studies [29, 63], to successfully capture the cyclic behaviour of the beam-to-column connections, the Chaboche model was used to simulate the strain hardening behaviour of the stainless steel. In this model, the following equation was used to the define the increase of yield surface:

$$\sigma^0 = \sigma|_0 + Q_\infty \left(1 - e^{b\varepsilon^p}\right) \tag{1}$$

in which the $\sigma|_0$ is the initial yielding stress when plastic strain is zero; Q_∞ represents the maximum change in the size of the yield surface; ε^p is the plastic strain; and b is parameter which determines the yield surface change rate with the plastic strain. In this study, the values of $\sigma|_0$, Q_∞ and b were calibrated to be equal to 150 [MPa], 500 [MPa] and 10 according to the experimental results, respectively.

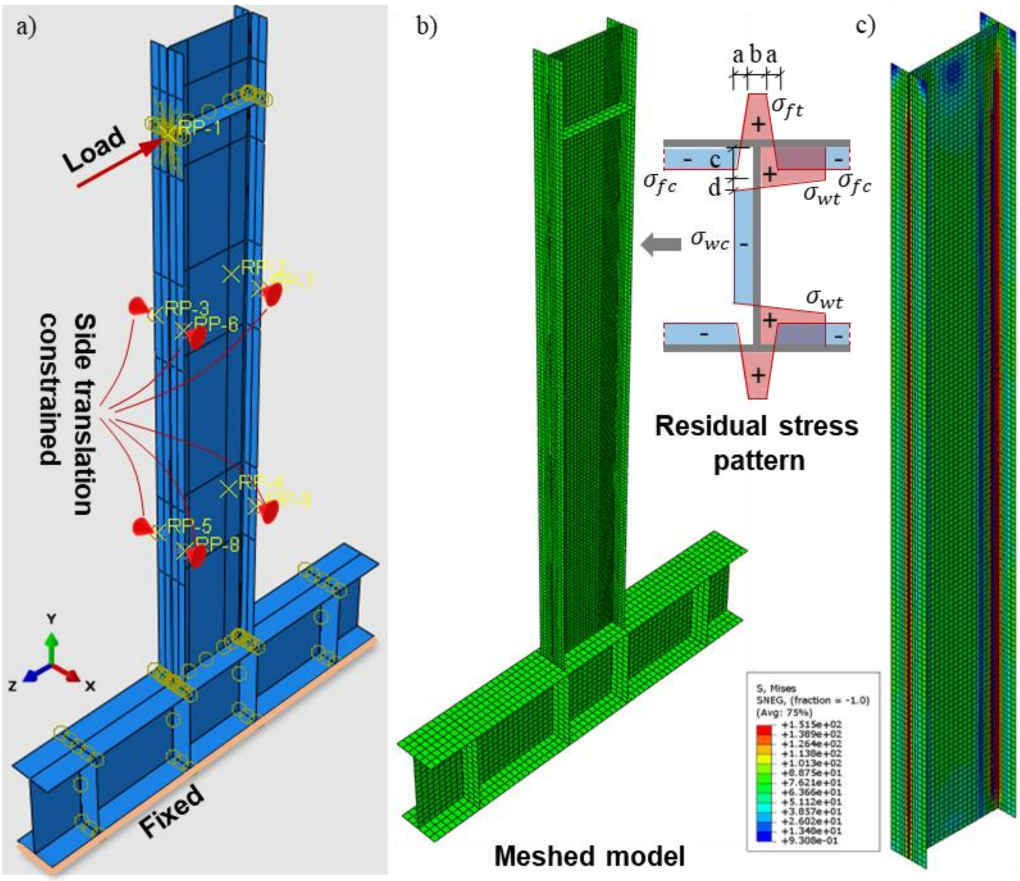

Fig. 7. FE model: a) constraints of the beam-to-column connection; b) meshed beam-to-column model; and c) residual stress analysis.

Existing studies have shown that significant residual welding stresses exist in welded members. Such residual welding stress could be close to the yield stress and thus could affect the flexural strength and the stability of steel members [64-66]. Therefore, a proper consideration of the residual tress in the finite element model should be made for an accurate simulation. In this study, the residual stress pattern shown in Fig. 7(b) is implemented based on [65]. It should be noted that the columns of the present study are much stiffer compared to the beams and no evident deformation was observed in the tested specimens. Hence, it was deemed adequate to consider residual stresses only in the beams of this study. The values of the residual stresses at different regions of the section are calculated according to Table 4 [65] and applied in the FE model as a predefined field in the plates of the beam (Fig. 7(b)). As can be observed, the maximum von Mises stress can reach as high as 151 MPa at the area close to the web-flange intersection point. As such, the cyclic behaviour of the joint is expected to be affected. Detailed description will be provided in the subsequent sections.

Table 4 Distribution parameters for the welding residual stress (symbols according to Fig. 7) [65].

$\sigma_{ft} = \sigma_{wt}$	$\sigma_{fc} = \sigma_{wc}$	a	b	c	d
$0.8\sigma_{0.2}$	$\sigma_{fc} = \dfrac{a+b}{w-(a+b)}\sigma_{ft}$ $\sigma_{wc} = \dfrac{2c+d}{h-2t_2-(2c+d)}\sigma_{wt}$	$0.225w$	$0.05b_f$	$0.025(h-2t_2)$	$0.025(h-2t_2)$

4. Result and discussion

4.1 Mesh convergency analysis

In order to find the optimal mesh scheme for the investigated connection, a mesh convergency analysis was conducted as shown in Fig. 8. As the residual stress varies along the flanges and webs, three mesh schemes considering different mesh size (N_i) in regions with distinct residual stress state are employed (Fig. 8a). For example, the flange with constant negative residual stress is divided into N_1 (equals 2, 4 and 6 for Mesh1, 2 and 3 respectively) elements. Besides, three element sizes (h = 12.5, 10, and 7.5 [mm]) in the length direction of the beam are considered. As shown in Figs. 8b and c, all three mesh schemes reached a very close predictions of the load-displacement curves and failure pattern which will be presented in detail in the subsequent sections. Therefore, to reduce the computational cost, the first mesh scheme (i.e., Mesh1) was used in all the simulations of this study.

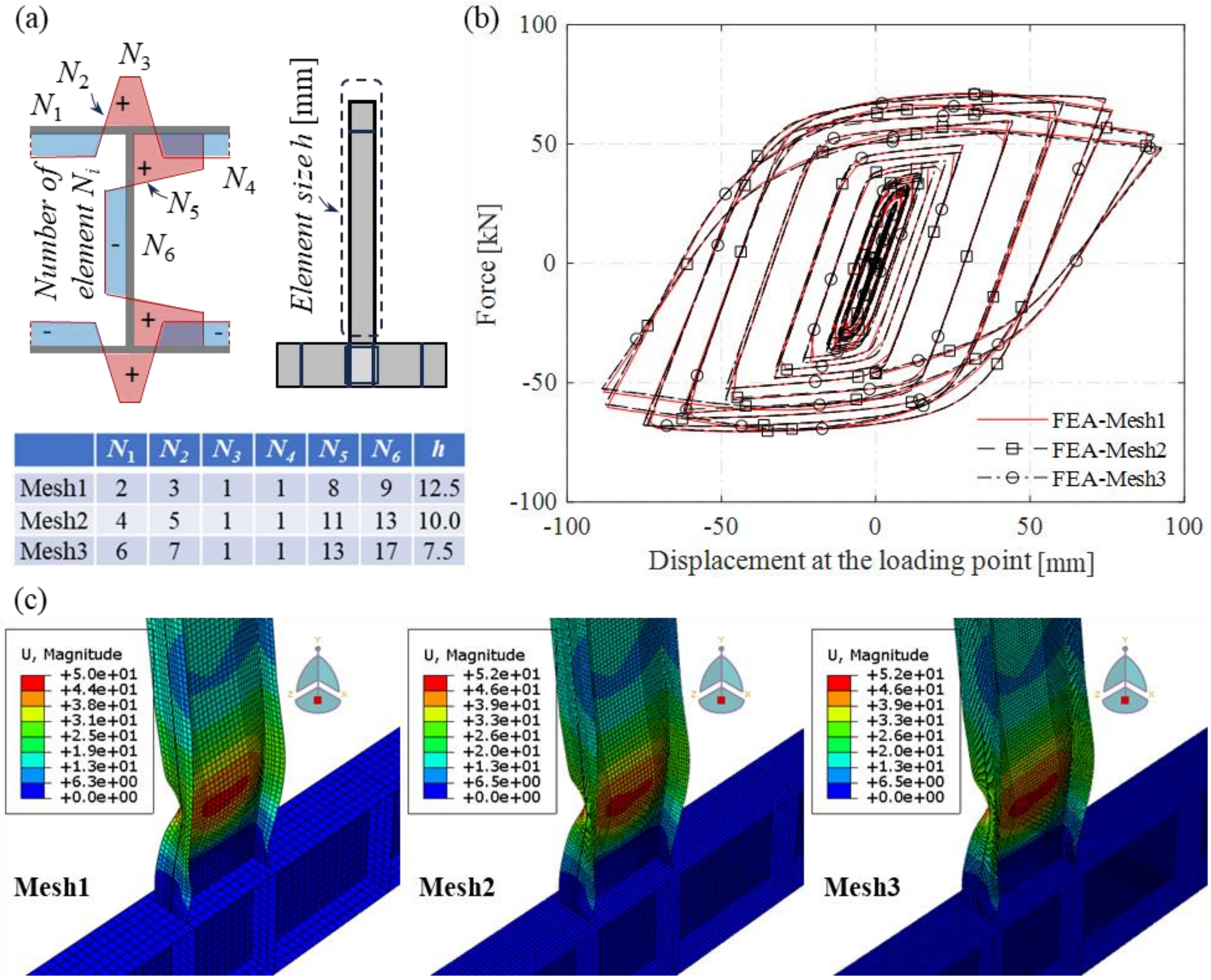

	N_1	N_2	N_3	N_4	N_5	N_6	h
Mesh1	2	3	1	1	8	9	12.5
Mesh2	4	5	1	1	11	13	10.0
Mesh3	6	7	1	1	13	17	7.5

Fig. 8. Mesh convergency analysis: (a) three mesh schemes; (b) comparison of load-displacement curves with three mesh schemes; (c) comparison of the eventual failure pattern with three mesh schemes.

4.2 Failure modes

During testing, the specimens were closely inspected to check if there was any buckling or localized failure. Due to the test set-up installation mistakes, Test-6 showed significant unexpected out-of-plane deformation that is omitted from discussion in this section. Results show that all specimens exhibited similar failure pattern. At initial loading stages (for rotation less than 0.01), there was no evidence of residual deformation. As the loading amplitude increased, increasing deformation of the web and flanges close to the bottom of the beam was observed. Upon buckling initiation, the deformation continued to increase. The number of loading cycles at which local buckling occurred were slightly different in each test. For Tests 1, 3 and 4, the local buckling of the flanges occurred at the second loading cycle of the sixth loading condition (denoted as LC6-2), while the web buckled at the second loading cycle of the eighth loading condition (denoted as LC8-2). However, for Tests 2 and 5, flange buckling occurred at the first loading cycle of the seventh loading condition (denoted as LC7-1), and the web buckling happened in the first and second loading cycle of the ninth loading condition respectively (denoted as LC9-1 and 2).

The deformation evolution during loading has also been successfully captured by the FE model. The numerical solutions of Test-1 with significant deformations are presented in Fig. 9. For clarity, only the deformed specimens at the load peaks of the last loading cycle are illustrated. As can be seen, global buckling and localised flange and web buckling occurred simultaneously at the second loading cycle of the eighth loading condition (LC8-2Pl) when the pull load was applied. After that, the deformation increased gradually. Similar failure process can also be found in the other tests.

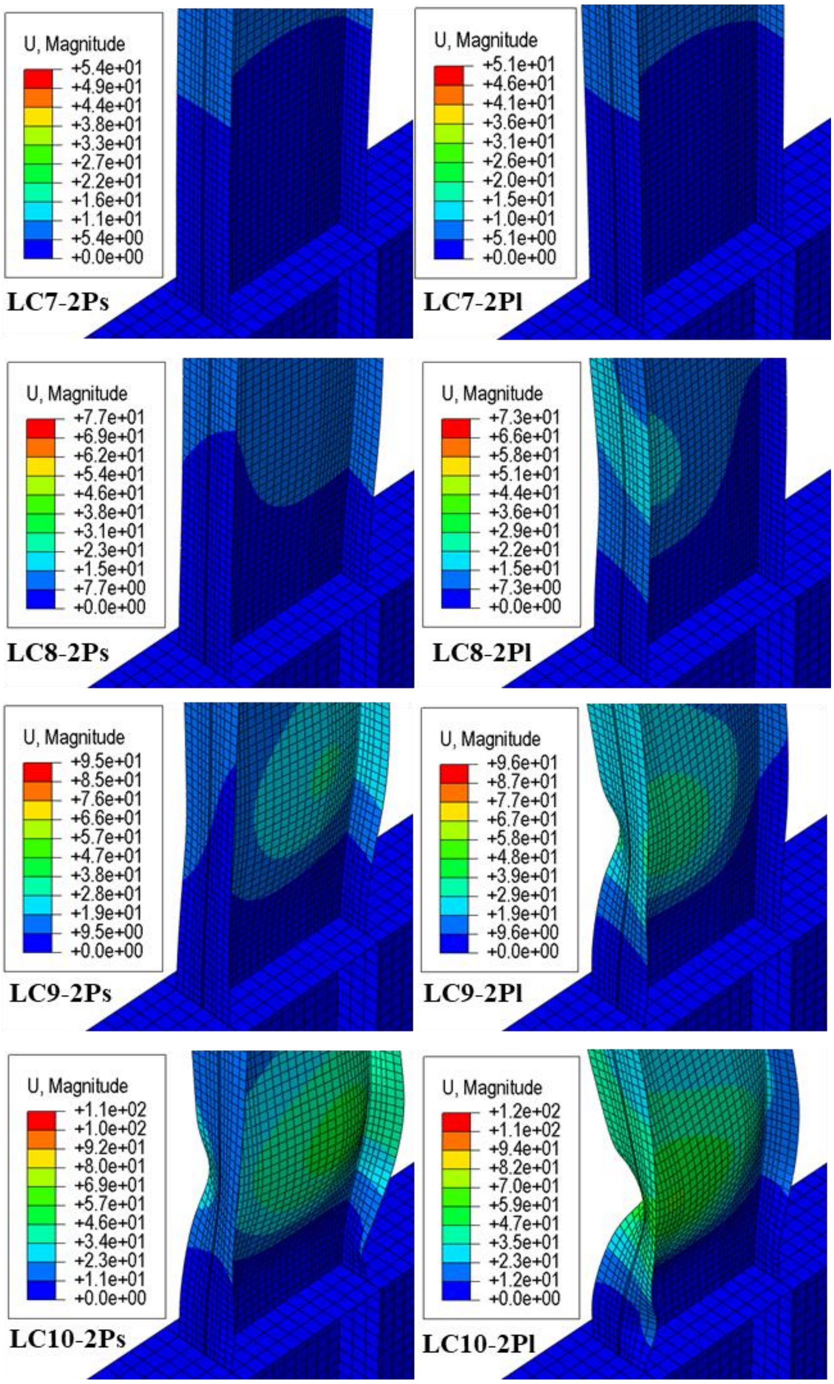

Fig. 9. Web and flange deformation process of Test-1 at selected stages based on FE model.

The ultimate failure modes from the tests and the finite element analysis (FEA) are shown in Fig. 10. Generally, a good agreement between the test and the FE model results is achieved. From both experimental and numerical results, it can be seen that the dominant failure mode is the combined global (flexural and torsional) and local (web and flanges) buckling of the beam. No material or welding fracture failure was observed. In addition, there were no signs of buckling within the horizontal member in both the test and numerical results. Therefore, it can be concluded that the governing failure of the welded stainless steel beam-to-column connection investigated in this study is the global and local buckling failure of the beam.

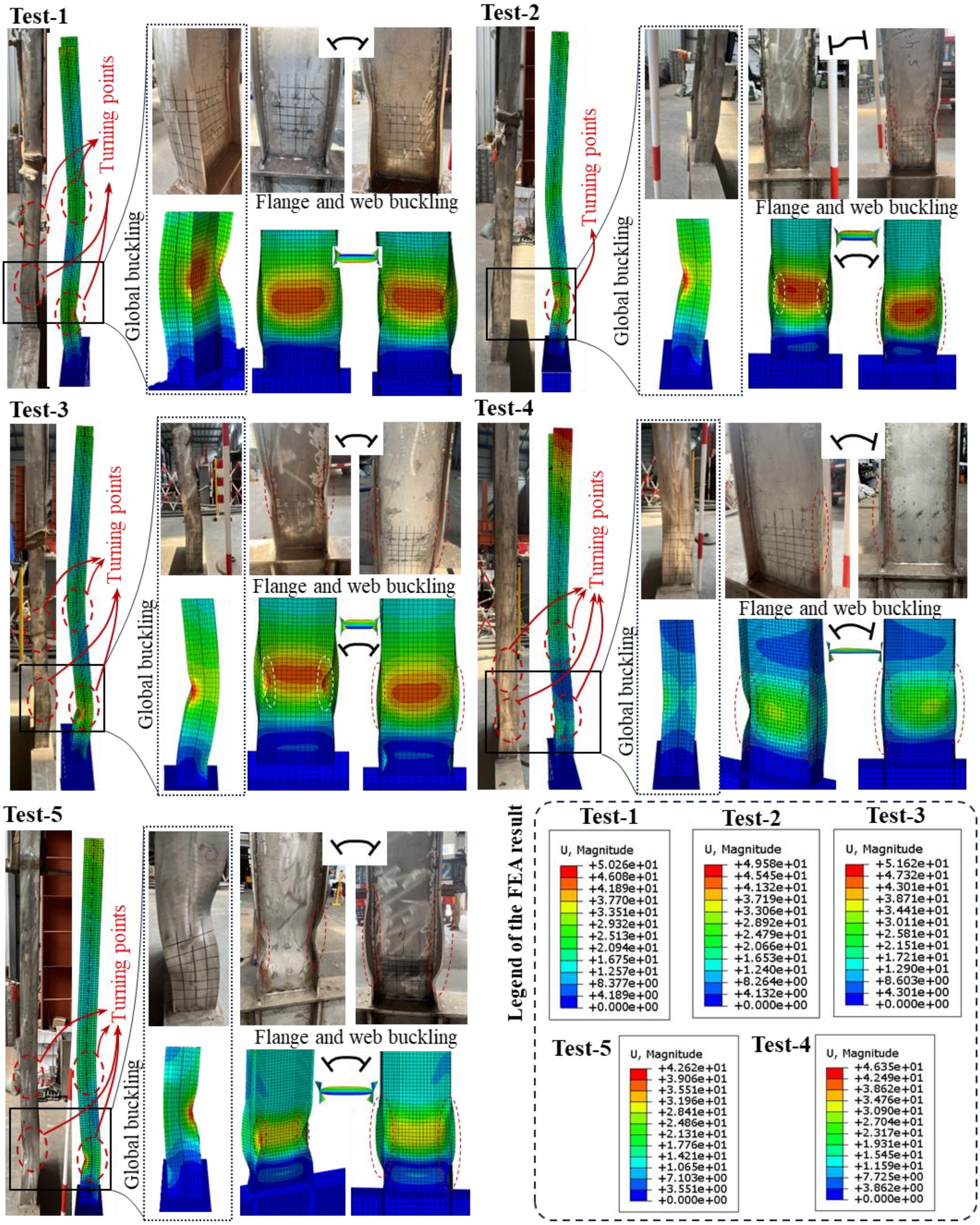

Fig. 10. Experimental and numerical failure modes.

Specifically for the global buckling, significant out-of-plane flexural deformation and in-plane torsional deformation can be observed in both test and FEA results. Affected by the side constraints, there are two turning points along the beam shown in the FEA results for all specimens and in failed specimen of Tests 1, 3, 4 and 5 (circled with red dashed line in Fig. 10). However, for Test 2, only one obvious turning point close to the beam-and-column intersection point was observed. Such difference might be attributed to the fact that Test 2 showed a significant global torsional buckling. As such, the contacting force between the beam and the side bracing is less significant compared to the other specimens. For the other tests, the flexural buckling was more significant. Therefore, the second turning point (the upper one) would appear due to the side constraint.

For the local buckling occurring at the web and flanges, excellent agreement between the tests and the FE models has been achieved, both in terms of buckling area and buckling shape. As shown in Fig. 10, the buckling area is mainly within the region of 300 [mm] above the beam-column intersection point. For Tests 1, 3-5, both flanges buckled in opposite direction and a half-sine-wave-like shape was observed in the web. The buckling shape was generally symmetric in these specimens. However, for Test 2, the web showed a sine-wave-like buckling shape and the flanges buckled towards the same direction. This discrepancy might be attributed to the initial anti-symmetric geometry imperfection pattern of the beam of Test 2, which, contrary to other tests, has led to a different failure pattern, with more torsional and less flexural deformations. Overall, the present FE model achieved a very good agreement with the test results.

4.3 Load-displacement behaviour

To further investigate the behaviour of the welded connections under quasi-static cyclic loading, the load-displacement and skeleton curves of all specimens are presented in Fig. 11. Moreover, the load-displacement curves obtained from the FEA results are also plotted in the same figure for comparison purposes. It should be noted that the displacements at the loading point were based on the measurements from the pull string. The FEA results showed generally good agreement with the test results. The peak value of the force in each loading cycle from the FEA results is generally slightly smaller than the test results and the discrepancy increases for higher displacements.

A pronounced hysteric behaviour can be observed in both the test and FEA results. In FEA results, the force appears to initially unload faster than that in the test results before reaching the reversed plastic region and then to be followed by slightly lower slope of the load-displacement curve. Such difference might be attributed to the error in the constitutive modelling of the stainless steel used in the present study. Since the experimental data of the cyclic behaviour of stainless steel used in this study is not available, the parameters used in the present work is calibrated through the overall hysteresis behaviour, failure mode and strain distribution of the investigated welded connection. Given more accurate constitutive parameters are available in the future, more accurate prediction of the load-displacement curve can be obtained. Nevertheless, both FEA and test results show that for specimens of the same group, i.e. with the same column but different cross-section for the beam, the shape of the load-displacement curve flattens as the beam section size reduces. This is expected as a smaller section leads to less stiffness and flexural capacity.

To better evaluate the results and compare the test and FEA results, the skeleton curves of all specimens are presented in Fig. 11(f). A hardening behaviour in which the force increases with displacement when the specimen enters the plastic range can be found from both FEA and test results. However, except Test 4, such hardening phenomenon is less significant at late stages of the cyclic loading. Moreover, for specimens of the same group (i.e. Tests 1-3 and Tests 4-5), the slope of the force-displacement curve in the elastic range decreases as the beam section size reduces, and the force in the plastic range from FEA results is smaller than that of the test results. For the tests with greater loading height (Tests 4-5), the skeleton curves show higher stiffness and load capacity for specimens with larger beam sections.

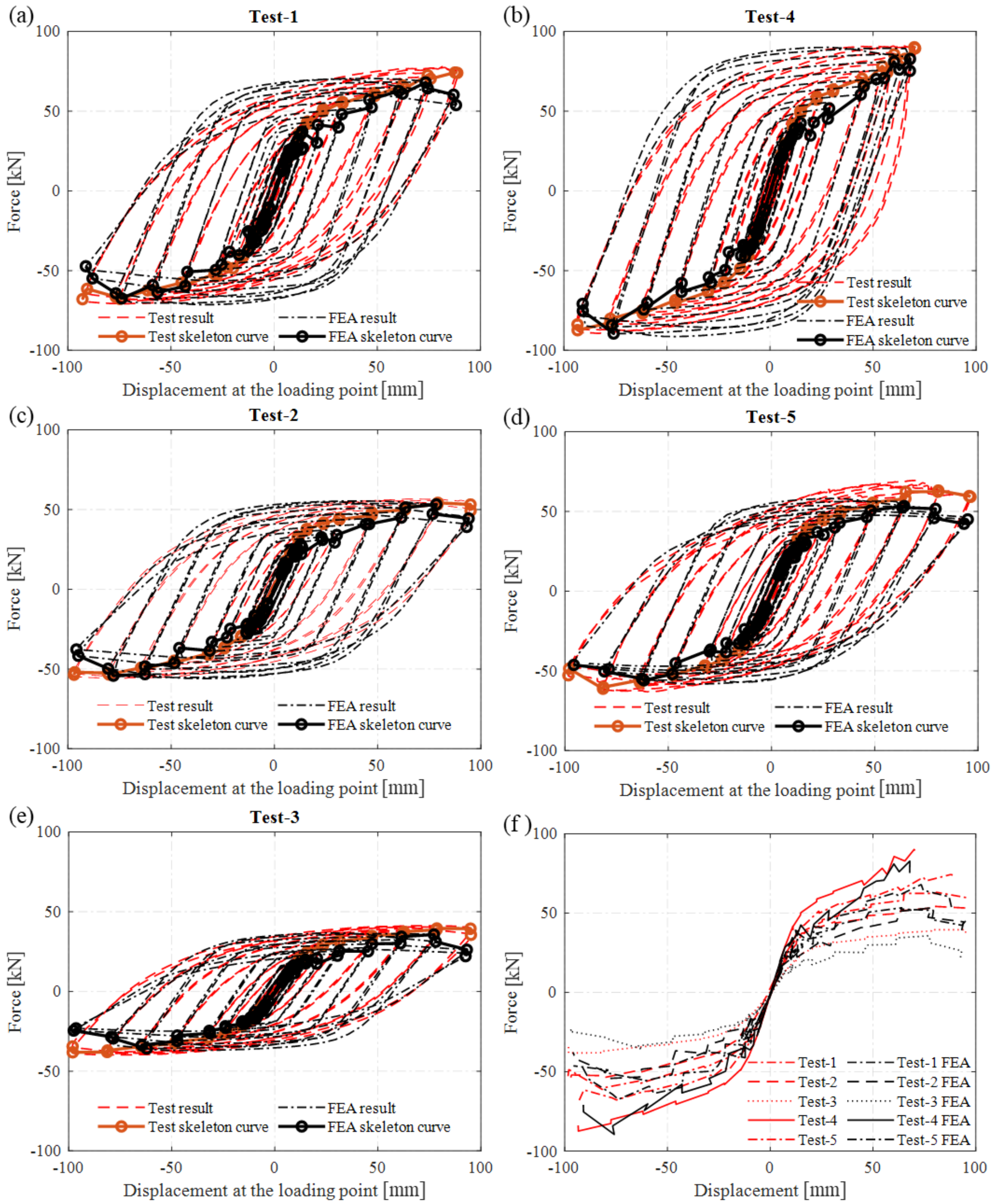

Fig. 11 (a)-(e) Load-displacement curves of Tests 1-5 and (f) skeleton curves.

From the above comparison between the test and FEA results, it can be briefly concluded that the developed FE models can predict the cyclic behaviour of the welded beam-to-column connections with reasonable accuracy. The load prediction from the FEA results is slightly smaller than that of the tests and the difference in the force increases with the displacement. This difference might be attributed to the friction between the beam and the side bracing of the test. As the flexural and torsional deformation increased during testing, the pressure between the beam and the side bracing increased significantly, resulting in a greater friction force. Hence, the slight variations between test and FEA might be related to this friction that has not been considered in FE models. Nevertheless, the present FE models can still be used to assist the investigation of the cyclic behaviour of the presented welded beam-to-column connection.

4.4 Strain distribution

Utilising the strain gauge measurements, the strain distribution of the beams has been developed. Due to space limitation, only the strain distribution at three sections close to the bottom of the beam in Test-1 is presented in Fig. 12 (black lines for positive and red lines for negative horizontal displacements of the beam). For the top (Figs. 12(a) and (d)) and middle sections (Figs. 12 (b) and (e)), the strain distribution along the steel section generally shows a linear distribution in the early loading cycles when the beam exhibits elastic behaviour. However, as local buckling occurs, the strain distribution on the flanges changes drastically and the strain on the whole section is not linearly distributed anymore. However, the strains on the web (i.e., recordings from strain gauges WN1-WN2-WN3, WN4-WN5-WN6, WS3-WS2-WS1, WS6-WS5-WS4) are still linearly distributed. As the number of loading cycle further increases, the strain distribution along the steel section becomes nonlinear due to the web buckling, which causes plastic deformation. It can also be observed that the strain on the south side of the web of the bottom section (Fig. 12(f)) is close to zero, as this section is very close to the welding line with the column, where the deformation of the beam is restrained and thus negligible. On the north web, strain develops as the location of the bottom section is slightly higher away from the welding line.

To further investigate the neutral-axis-change behaviour, the strain distribution in Test-1 from the FEA results is also presented in Fig. 13 for comparison. Thus, the strain distribution at the last loading cycle of each cycle type is presented. It should be noted that as shell elements have been adopted in the FEA, the strain gradient in the thickness direction is not considered. Therefore, for each row of strain gauges, only one graph is plotted. Nevertheless, the comparison between the test and FEA results is justified by the fact that the beam is subjected to in-plane bending before the occurrence of global and local buckling, hence the out-of-plane bending effect and thus strain gradient can be ignored at this stage. The strain distribution pattern on the transverse direction of the FEA results shown in Fig. 13 is similar to the corresponding one of the tests in Fig. 12. Before the occurrence of global and local buckling, a linear strain distribution can be observed and after that, the strain distribution becomes nonlinear due to plastic deformation.

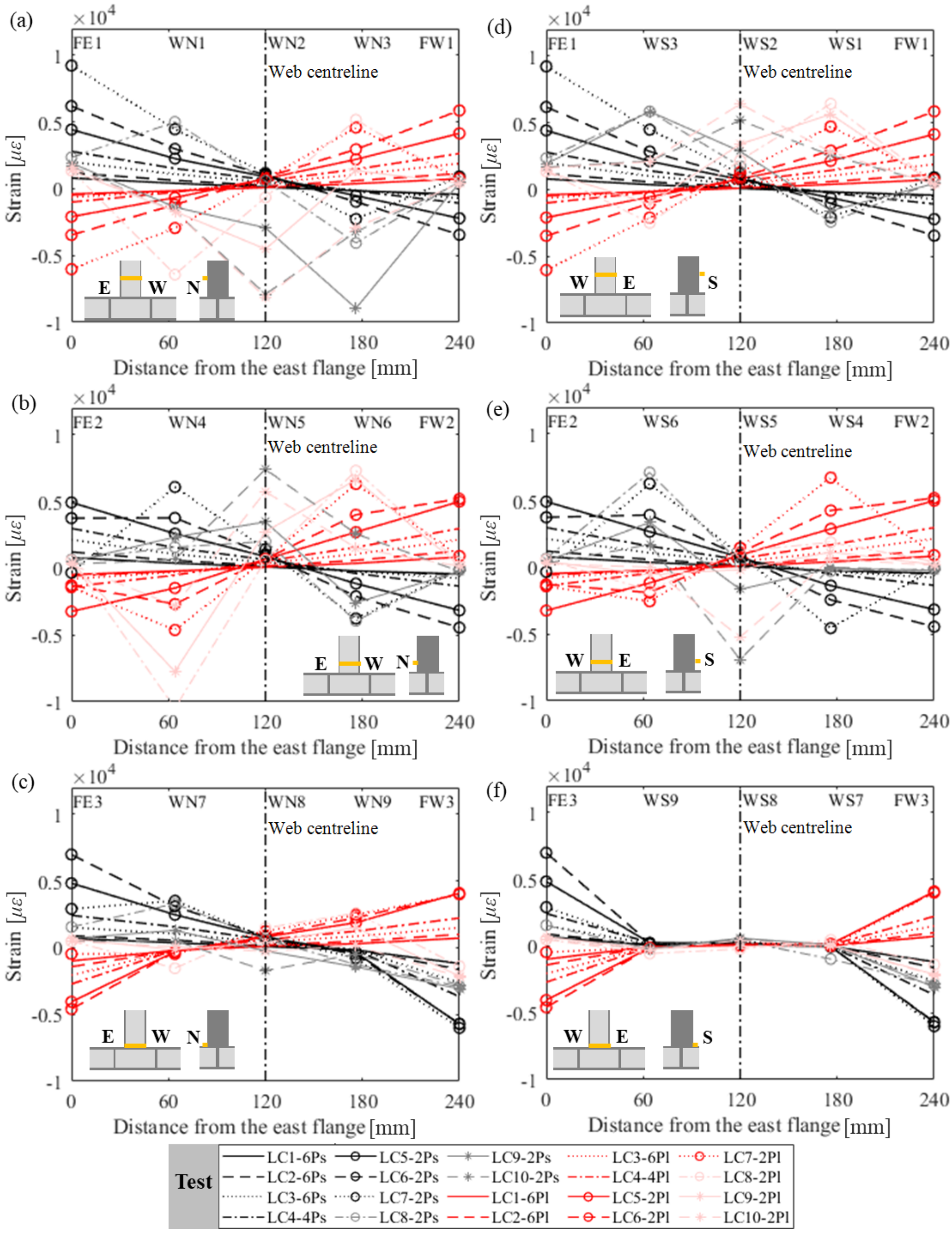

Fig. 12. Experimental strain distribution of the beam in Test 1.

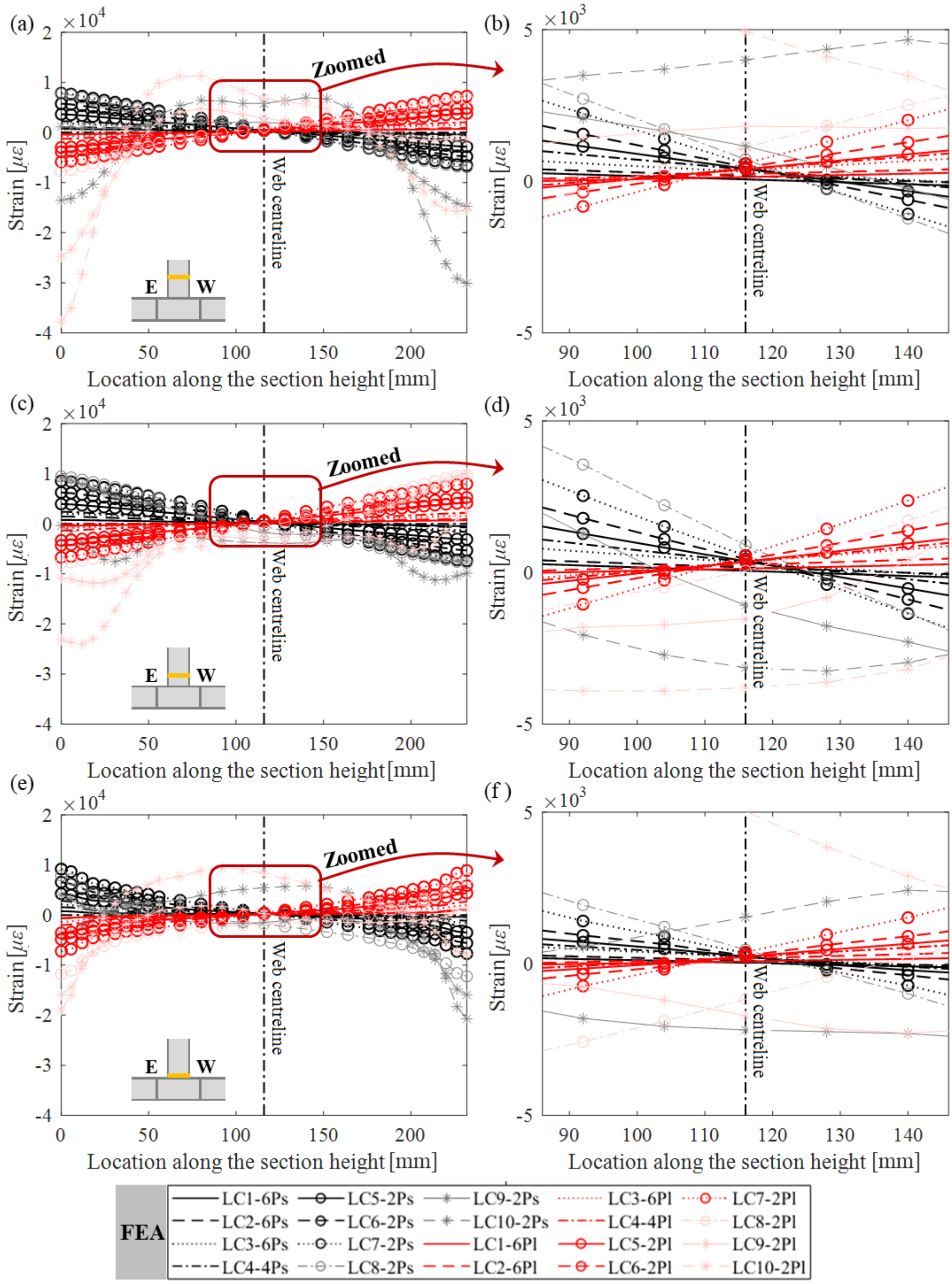

Fig. 13. Numerical strain distribution of beam in Test 1.

Analysing the experimental strain data, the position of the neutral axis of the beam can also be identified. It is worth noticing that the neutral axis, i.e., position of zero strain, is not located in the centroid of the web and its position changes with the cyclic loading. Specifically, when a pushing load is applied, the neutral axis is greater than 120 [mm] from the further fibre of the east flange. When the loading is reversed, the neutral axis switches to the other side of the centreline of the web. Similar observations were made in all specimens except Test 2 which exhibited a distinct failure mode. To further investigate the neutral-axis-change phenomenon, the location of the neutral axis of all tested specimens is presented in Fig.

14. In this figure, the horizontal axis represents the half loading cycle when a push or pull load was applied. The position of the neutral axis was obtained by finding the position of zero strain through a linear regression of the strain reading on the web. Each marker in the figure represents the position of the neutral axis determined by one row of strain gauges on both sides of the web. It is obvious that the distance between the obtained neutral axis position and the web's centreline are different at different sections (North Rows 1-3 and South Rows 1-3). In most cases, the location of neutral axis alternates between the two sides of the web at the beginning of the cyclic loading. In the meantime, the distance between the neutral axis and the centreline of the web initially increases with the loading cycle and then decreases abruptly when web buckling occurs. At a certain stage, the position of the neutral axis when push and pull loading applied switches until the end of the test.

Likewise, the position of the neutral axis from the FEA results is determined and plotted in Fig. 15. It is evident that the neutral axis firstly moves away from and then towards the web centreline (the horizontal dashed line in the figure). This is also shown from the zoomed-in figures (Fig. 13 (b), (d), and (f)) that clearly demonstrate that the neutral axis position also changes. Apparently, in the early loading stages, the neutral axis is not in the centre of the web, which means there is somewhat non-symmetricity in the section when load is applied. Such non-symmetricity is found to be caused by the plastic deformation in the section. As shown in Fig. 7, the welding residual stress is as high as 151 MPa and symmetric with respect to the web centreline. When the external force is applied, part of the sections close to the bottom of the beam has entered the plastic region (Fig. 16). While loading, section zones subjected to tensile stress caused by the external force will be further loaded, whereas the remaining zone of the section will be unloaded. As stainless steel exhibits significant non-linearity thus the unloading and reloading stiffnesses are different. As such, the neutral axis would move to the side having greater stiffness. Specifically, when the pushing load is applied, the stainless steel in the east side will be further loaded and that in the west side will be unloaded. As the unloading stiffness is close to the elastic stiffness which is significantly greater than the stiffness in the plastic region. As a result, the neutral axis is towards the west side. When the external load direction is reversed (from pushing to pulling), the unloading stiffness in the east side of the beam will be greater than that in the west side as part of the stainless steel in this side will be loaded to the plastic region. As such, the neutral axis will move towards the east side. This phenomenon indicates that the influence of residual stress should be considered, while predicting and designing flexural performance of the welded stainless steel members.

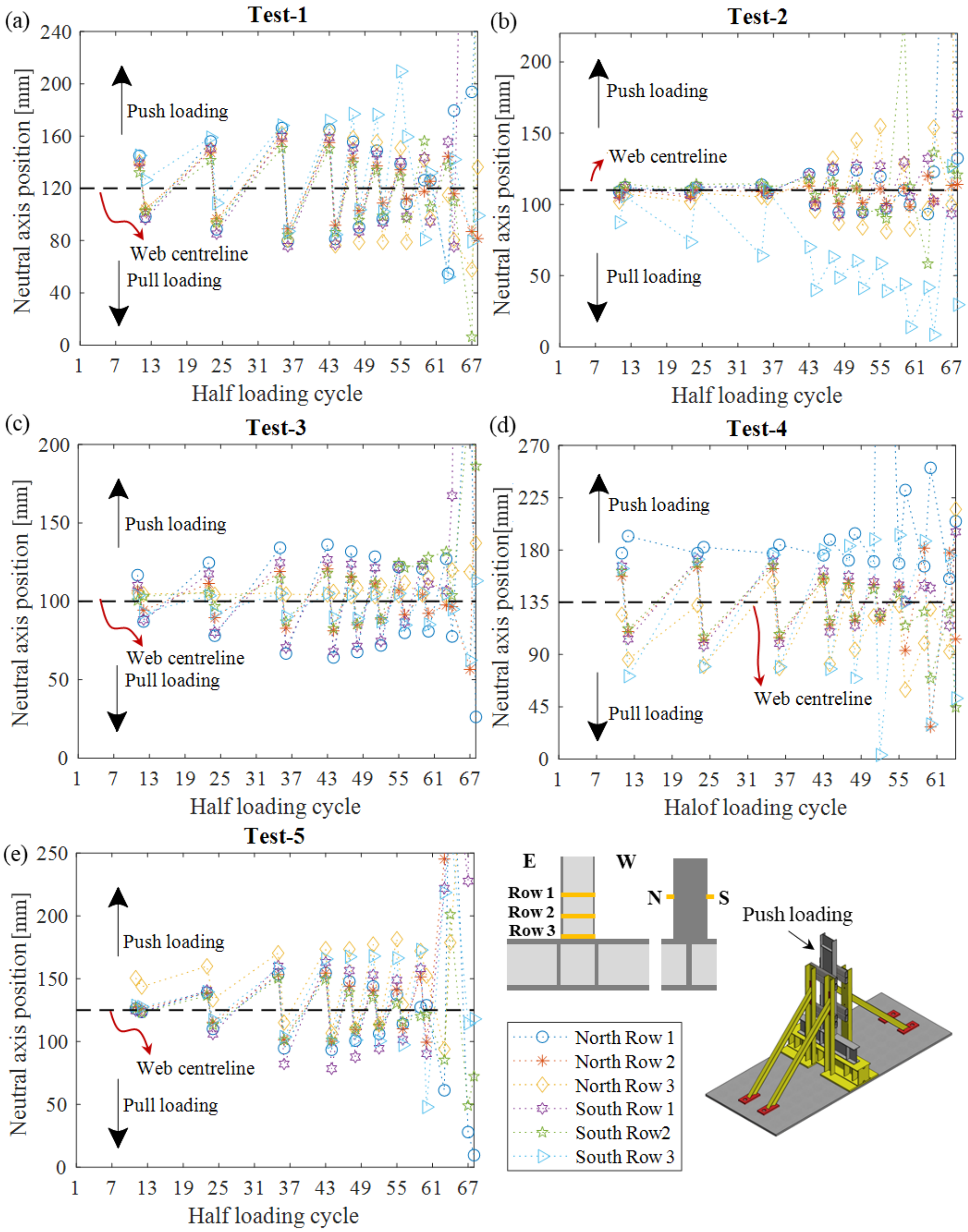

Fig. 14. The neutral axis position of each specimen from test results.

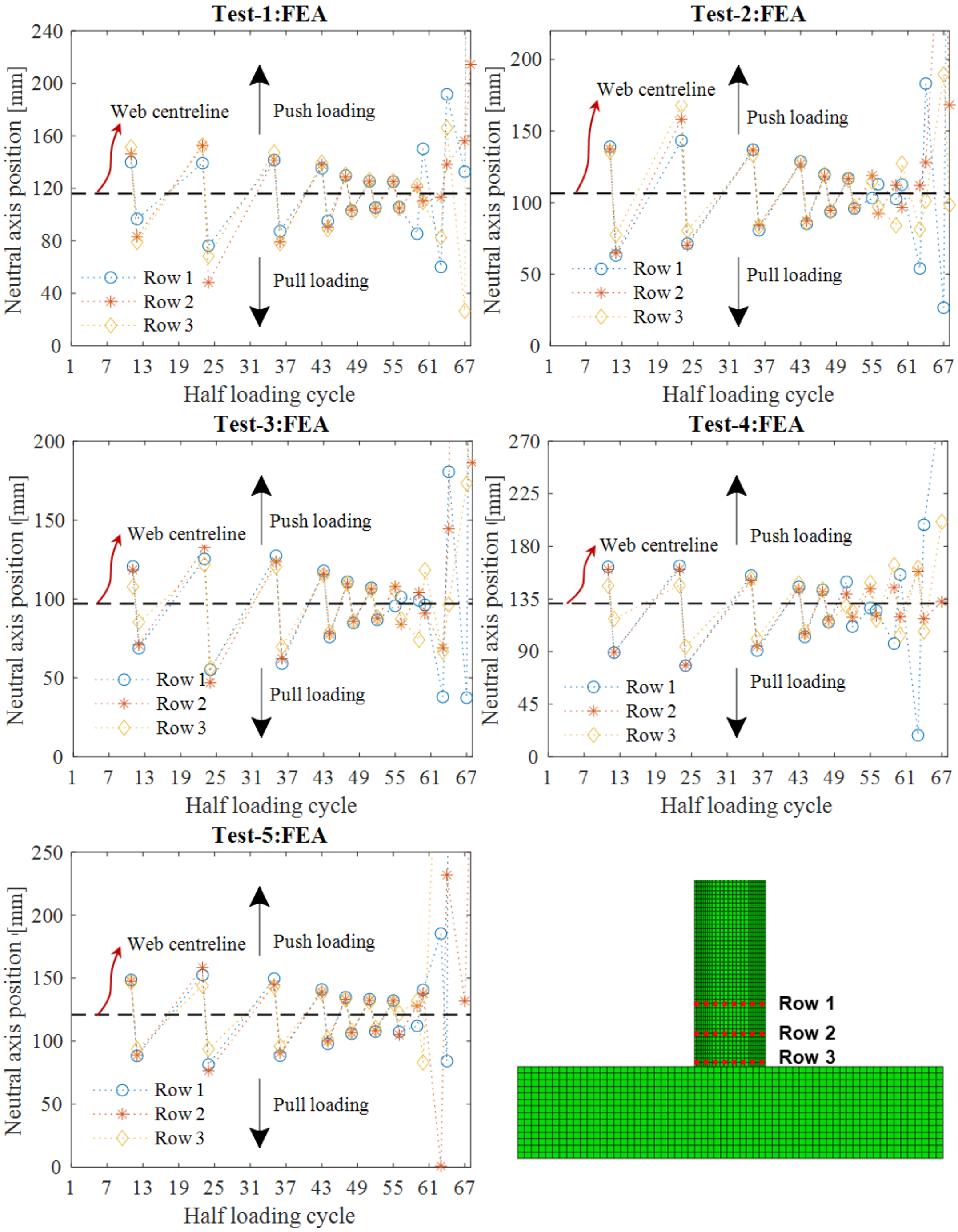

Fig. 15. The position of neutral axis of each test from FEA results.

Fig. 16. Plastic strain in the web at different loading cycles.

4.5 Energy dissipation

To evaluate the energy dissipation of the welded stainless steel connections under cyclic loading, the area enclosed by the load-displacement curve in each cycle is calculated and presented in Fig. 17. Results from FEA are also plotted in the same figure for comparison. A similar trend regarding the energy dissipation is observed between the FEA and test results with the latter being generally a bit lower. As previously discussed, the differences between test and FEA results might be related to the experimental friction forces between the beam and the side bracing during loading. As such, part of the energy could have been converted into heat during the test and the energy dissipated by the plastic deformation of the welded connections appeared to be smaller for the test compared to the FEA.

Nevertheless, in both test and FEA results, it can be seen that before the 20^{th} loading cycles (i.e., when the applied rotating angle is less than 0.01), the dissipated energy is almost zero, which indicates the plastic deformation in such loading cases is insignificant. After that, the dissipated energy increases as the load increases. For the specimens in the same group, i.e., Tests 1-3 and Tests 4-5, the energy dissipation capacity generally decreases with the section size. Therefore, a larger sectional size has led to a better performance in terms of the energy dissipation when subjected to cyclic loading.

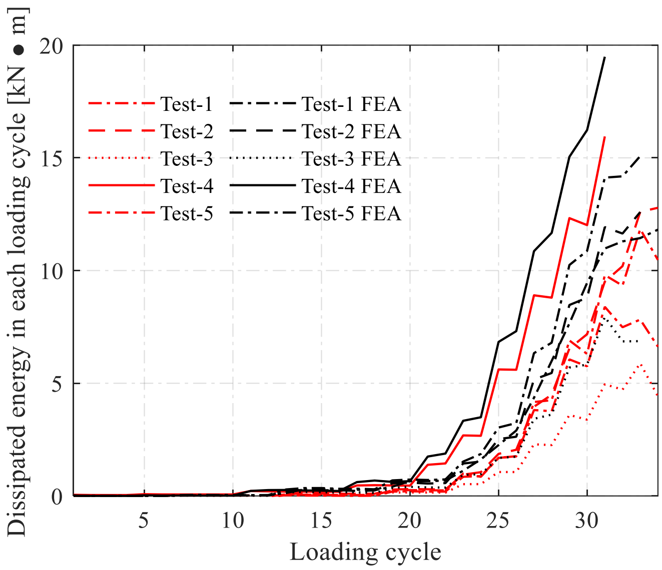

Fig. 17. Dissipated energy based on test and FEA results.

4.6 Practical consequences for connection design

From the present experimental and numerical study, it can be found that the failure mode of the welded stainless steel beam-to-column connection is buckling of the beam, no fracture failure of the stainless steel and welding was observed. Such observation indicates that in the practical design, more attention should be given to the flexural behaviour of the beam such that the global and localized buckling of the beam can be avoided. Besides, the load-displacement behaviour of the investigated connection showed a good hysteric performance, which makes the welding stainless steel connection a promising component while designing MRF with seismic risks. However, the neutral axis was found change under cyclic loading due to the high-amplitude welding residual stress. Such change could affect the cyclic behaviour prediction of the welded stainless steel beam-to-column connections. More research should be conducted in the future to propose a reasonable design method such that the effect of residual stress can be properly considered.

5. Conclusions

In this study, six welded stainless steel beam-to-column connections were experimentally tested and numerically simulated under cyclic loading. The deformation process, load-displacement curves, sectional strain distribution close to the bottom of the beam and the energy dissipation capacity were investigated and discussed. Based on the experimental observations and FEA results, the following conclusions can be drawn:

1. Compared to the test results, the present FE model allows for a reasonably accurate prediction of the cyclic behaviour of the investigated stainless steel beam-to-column connections in terms of the failure mode, load-displacement curve and the flexural behaviour of the beam.
2. The dominant failure mode of the welded stainless steel beam-to-column connections is the combined global flexural and torsional buckling and localised web and flange buckling. No failure in the stainless steel and the welding were observed in the test.
3. The force prediction from the FEA results is generally smaller than that of the test results.
4. The energy dissipation determined from the FEA results is greater than that of the test results. The reason for such discrepancy might be attributed to the friction between the beam and the side bracing.
5. The position of the beam's neutral axis is significantly affected by the residual welding stress. While subjected to cyclic loading, the neutral axis position could change as different regions would experience loading and unloading with different stiffness. Such influence should be considered while designing such connections up to future.

Acknowledgements

The research work presented in this paper was supported by Research England under the QR Global Challenges Research Fund (Grant Ref: 956FET). This financial support is gratefully acknowledged. The authors thank the technicians of the School of Civil Engineering at Central South University for their valuable assistance during the experimental programme.

References

[1] N.R. Baddoo, Stainless steel in construction: A review of research, applications, challenges and opportunities, Journal of Constructional Steel Research 64(11) (2008) 1199-1206. https://doi.org/10.1016/j.jcsr.2008.07.011.
[2] L. Gardner, Stability and design of stainless steel structures – Review and outlook, Thin-Walled Structures 141 (2019) 208-216. https://doi.org/10.1016/j.tws.2019.04.019.
[3] L. Yang, M. Zhao, T.-M. Chan, F. Shang, D. Xu, Flexural buckling of welded austenitic and duplex stainless steel I-section columns, Journal of Constructional Steel Research 122 (2016) 339-353. https://doi.org/10.1016/j.jcsr.2016.04.007.
[4] F. Zhou, L. Li, Experimental study on hysteretic behavior of structural stainless steels under cyclic loading, Journal of Constructional Steel Research 122 (2016) 94-109. https://doi.org/10.1016/j.jcsr.2016.03.006.
[5] Y. Bu, Y. Wang, Y. Zhao, Study of stainless steel bolted extended end-plate joints under seismic loading, Thin-Walled Structures 144 (2019) 106255. https://doi.org/10.1016/j.tws.2019.106255.
[6] L. Lázaro, R. Chacón, Material behaviour of austenitic stainless steel subjected to cyclic and arbitrary loading, J. Constr. Steel Res. 189 (2022) 107113. https://doi.org/10.1016/j.jcsr.2021.107113.
[7] I. González-de-León, I. Arrayago, E. Real, E. Nastri, Rotation capacity of cold-formed stainless steel RHS beams under cyclic loading, Journal of Constructional Steel Research 192 (2022) 107199. https://doi.org/10.1016/j.jcsr.2022.107199.
[8] L. Gardner, D.A. Nethercot, Experiments on stainless steel hollow sections—Part 2: Member behaviour of columns and beams, Journal of Constructional Steel Research 60(9) (2004) 1319-1332.

https://doi.org/10.1016/j.jcsr.2003.11.007.
[9] M. Theofanous, L. Gardner, Testing and numerical modelling of lean duplex stainless steel hollow section columns, Engineering Structures 31(12) (2009) 3047-3058. https://doi.org/10.1016/j.engstruct.2009.08.004.
[10] H.X. Yuan, Y.Q. Wang, L. Gardner, X.X. Du, Y.J. Shi, Local–overall interactive buckling behaviour of welded stainless steel I-section columns, Journal of Constructional Steel Research 111 (2015) 75-87. https://doi.org/10.1016/j.jcsr.2015.04.003.
[11] Y. Sun, A. He, Y. Liang, O. Zhao, Flexural buckling behaviour of high-chromium stainless steel welded I-section columns, Thin-Walled Structures 154 (2020) 106812. https://doi.org/10.1016/j.tws.2020.106812.
[12] F. Zhou, L. Huang, H.-T. Li, Cold-formed stainless steel SHS and RHS columns subjected to local-flexural interactive buckling, Journal of Constructional Steel Research 188 (2022) 106999. https://doi.org/10.1016/j.jcsr.2021.106999.
[13] Y. Wang, L. Yang, B. Gao, Y. Shi, H. Yuan, Experimental study of lateral-torsional buckling behavior of stainless steel welded I-section beams, International Journal of Steel Structures 14(2) (2014) 411-420. https://doi.org/10.1007/s13296-014-2019-8.
[14] Y. Bu, L. Gardner, Local stability of laser-welded stainless steel I-sections in bending, Journal of Constructional Steel Research 148 (2018) 49-64. https://doi.org/10.1016/j.jcsr.2018.05.010.
[15] S. Li, L. Zhang, Y. Liang, O. Zhao, Experimental and numerical investigations of hot-rolled stainless steel channel section columns susceptible to flexural buckling, Thin-Walled Structures 164 (2021) 107791. https://doi.org/10.1016/j.tws.2021.107791.
[16] X.W. Chen, H.X. Yuan, X.X. Du, Z.W. Zhu, Nonlinear deformation behaviour and design of welded stainless steel I-section flexural members, Engineering Structures 252 (2022) 113683. https://doi.org/10.1016/j.engstruct.2021.113683.
[17] L. Li, H.-T. Li, B. Young, Cold-formed ferritic stainless steel SHS and RHS beams: Testing, modeling and design, Journal of Constructional Steel Research 197 (2022) 107429. https://doi.org/10.1016/j.jcsr.2022.107429.
[18] L. Gardner, Y. Bu, M. Theofanous, Laser-welded stainless steel I-sections: Residual stress measurements and column buckling tests, Engineering Structures 127 (2016) 536-548. https://doi.org/10.1016/j.engstruct.2016.08.057.
[19] Y. Bu, L. Gardner, Laser-welded stainless steel I-section beam-columns: Testing, simulation and design, Engineering Structures 179 (2019) 23-36. https://doi.org/10.1016/j.engstruct.2018.09.075.
[20] L. Yang, M. Zhao, L. Gardner, K. Ning, J. Wang, Member stability of stainless steel welded I-section beam-columns, Journal of Constructional Steel Research 155 (2019) 33-45. https://doi.org/10.1016/j.jcsr.2018.12.022.
[21] Y. Sun, Y. Liang, O. Zhao, B. Young, Cross-Sectional Behavior of Austenitic Stainless Steel Welded I-Sections under Major-Axis Combined Loading, Journal of Structural Engineering 147(12) (2021) 04021202. https://doi.org/10.1061/(ASCE)ST.1943-541X.0003175.
[22] Y. Sun, A. Su, K. Jiang, Y. Liang, O. Zhao, Testing, numerical modelling and design of stainless steel welded I-sections under minor-axis combined loading, Engineering Structures 243 (2021) 112513. https://doi.org/10.1016/j.engstruct.2021.112513.
[23] Y. Sun, K. Jiang, Y. Liang, O. Zhao, Experimental and numerical studies of high-chromium stainless steel welded I-section beam-columns, Engineering Structures 236 (2021) 112065. https://doi.org/10.1016/j.engstruct.2021.112065.
[24] S. Li, L. Zhang, O. Zhao, Global buckling and design of hot-rolled stainless steel channel section beam–columns, Thin-Walled Structures 170 (2022) 108433. https://doi.org/10.1016/j.tws.2021.108433.
[25] K.H. Nip, L. Gardner, C.M. Davies, A.Y. Elghazouli, Extremely low cycle fatigue tests on structural carbon steel and stainless steel, Journal of Constructional Steel Research 66(1) (2010) 96-110. https://doi.org/10.1016/j.jcsr.2009.08.004.

[26] Y.Q. Wang, T. Chang, Y.J. Shi, H.X. Yuan, L. Yang, D.F. Liao, Experimental study on the constitutive relation of austenitic stainless steel S31608 under monotonic and cyclic loading, Thin-Walled Structures 83 (2014) 19-27. https://doi.org/10.1016/j.tws.2014.01.028.

[27] S. Zheng, F. Zhou, J. Cheng, H.-T. Li, R. Rong, Experimental study on cyclic hardening characteristics of structural stainless steels, Journal of Constructional Steel Research 191 (2022) 107196. https://doi.org/10.1016/j.jcsr.2022.107196.

[28] K.H. Nip, L. Gardner, A.Y. Elghazouli, Cyclic testing and numerical modelling of carbon steel and stainless steel tubular bracing members, Eng. Struct. 32(2) (2010) 424-441. https://doi.org/10.1016/j.engstruct.2009.10.005.

[29] F. Zhou, C. Fang, Y. Chen, Experimental and numerical studies on stainless steel tubular members under axial cyclic loading, Eng. Struct. 171 (2018) 72-85. https://doi.org/10.1016/j.engstruct.2018.05.093.

[30] K.Y. Ning, L. Yang, H.Y. Ban, Y.N. Sun, Experimental and numerical studies on hysteretic behaviour of stainless steel welded box-section columns, Thin-Walled Structures 136 (2019) 280-291. https://doi.org/10.1016/j.tws.2018.12.038.

[31] R. Kim, T. Kim, S. Im, Y. Xi, Hysteretic behavior comparison of austenitic and lean duplex stainless steel square hollow section members under cyclic axial loading, Engineering Structures 237 (2021) 112227. https://doi.org/10.1016/j.engstruct.2021.112227.

[32] I. González-de-León, E. Nastri, I. Arrayago, R. Montuori, V. Piluso, E. Real, Experimental study on stainless steel tubular members under cyclic loading, Thin-Walled Structures 181 (2022) 109969. https://doi.org/10.1016/j.tws.2022.109969.

[33] C. Fang, F. Zhou, C. Luo, Cold-formed stainless steel RHSs/SHSs under combined compression and cyclic bending, J. Constr. Steel Res. 141 (2018) 9-22. https://doi.org/10.1016/j.jcsr.2017.11.001.

[34] K. Ning, L. Yang, H. Ban, Seismic Performance of Welded Stainless Steel H-Section Columns under Cyclic Horizontal Loading, Journal of Structural Engineering 147(4) (2021) 04021016. https://doi.org/10.1061/(ASCE)ST.1943-541X.0002958.

[35] Y. Chen, F. Zhou, R. Zhang, Y. Cai, Experimental study on seismic behavior of welded H-section stainless steel beam-columns, Eng. Struct. 259 (2022) 114105. https://doi.org/10.1016/j.engstruct.2022.114105.

[36] Y. Chen, F. Zhou, S. Zheng, J. Li, C. Shang, X. Lin, Influence of cyclic hardening characteristic on seismic performance of welded austenitic stainless steel H-section beam-column, Eng. Struct. 288 (2023) 116210. https://doi.org/10.1016/j.engstruct.2023.116210.

[37] L. Possidente, F. Freddi, N. Tondini, Dynamic increase factors for progressive collapse analysis of steel structures considering column buckling, Eng. Failure Anal. 160 (2024) 108209. https://doi.org/10.1016/j.engfailanal.2024.108209.

[38] Y. Sun, Y. Liang, O. Zhao, Testing, numerical modelling and design of S690 high strength steel welded I-section stub columns, J. Constr. Steel Res. 159 (2019) 521-533. https://doi.org/10.1016/j.jcsr.2019.05.014.

[39] A. Bouchaïr, J. Averseng, A. Abidelah, Analysis of the behaviour of stainless steel bolted connections, J. Constr. Steel Res. 64(11) (2008) 1264-1274. https://doi.org/10.1016/j.jcsr.2008.07.009.

[40] M.J. Hasan, M. Ashraf, B. Uy, Moment-rotation behaviour of top-seat angle bolted connections produced from austenitic stainless steel, J. Constr. Steel Res. 136 (2017) 149-161. https://doi.org/10.1016/j.jcsr.2017.05.014.

[41] M.J. Hasan, S. Al-Deen, M. Ashraf, Behaviour of top-seat double web angle connection produced from austenitic stainless steel, Journal of Constructional Steel Research 155 (2019) 460-479. https://doi.org/10.1016/j.jcsr.2018.12.015.

[42] M. Elflah, M. Theofanous, S. Dirar, Behaviour of stainless steel beam-to-column joints-part 2: Numerical modelling and parametric study, J. Constr. Steel Res. 152 (2019) 194-212. https://doi.org/10.1016/j.jcsr.2018.04.017.

[43] M. Elflah, M. Theofanous, S. Dirar, H. Yuan, Behaviour of stainless steel beam-to-column joints — Part 1:

Experimental investigation, J. Constr. Steel Res. 152 (2019) 183-193. https://doi.org/10.1016/j.jcsr.2018.02.040.
[44] M. Elflah, M. Theofanous, S. Dirar, H. Yuan, Structural behaviour of stainless steel beam-to-tubular column joints, Eng. Struct. 184 (2019) 158-175. https://doi.org/10.1016/j.engstruct.2019.01.073.
[45] Eurocode, Eurocode 3: Design of steel structures-Part 1-8: Design of joints. EN 1993-1-8, 3 ed., European Standard (CEN), Brussels, Belgium, 2005.
[46] O. Yapici, M. Theofanous, H. Yuan, K. Skalomenos, S. Dirar, Experimental study of ferritic stainless steel bolted T-stubs under monotonic loading, Journal of Constructional Steel Research 183 (2021) 106761. https://doi.org/10.1016/j.jcsr.2021.106761.
[47] H.X. Yuan, J.D. Gao, M. Theofanous, L. Yang, B.W. Schafer, Initial stiffness and plastic resistance of bolted stainless steel T-stubs in tension, Journal of Constructional Steel Research 173 (2020) 106239. https://doi.org/10.1016/j.jcsr.2020.106239.
[48] O. Yapici, M. Theofanous, H. Yuan, S. Dirar, S. Afshan, Numerical simulation and design of ferritic stainless steel bolted T-stubs in tension, Journal of Constructional Steel Research 198 (2022) 107555. https://doi.org/10.1016/j.jcsr.2022.107555.
[49] H.X. Yuan, X.H. Liu, J.L. Liu, M. Theofanous, Cyclic behaviour and hysteretic model of austenitic stainless steel bolted T-stubs, J. Constr. Steel Res. 182 (2021) 106659. https://doi.org/10.1016/j.jcsr.2021.106659.
[50] J.D. Gao, X.X. Du, H.X. Yuan, M. Theofanous, Hysteretic performance of stainless steel double extended end-plate beam-to-column joints subject to cyclic loading, Thin-Walled Struct. 164 (2021) 107787. https://doi.org/10.1016/j.tws.2021.107787.
[51] J.D. Gao, H.X. Yuan, H. Qian, X.W. Chen, Structural behaviour and design of stainless steel end-plate beam-to-exterior column minor-axis joints, Thin-Walled Structures 181 (2022) 110119. https://doi.org/10.1016/j.tws.2022.110119.
[52] L. Di Sarno, A.S. Elnashai, D.A. Nethercot, Seismic performance assessment of stainless steel frames, Journal of Constructional Steel Research 59(10) (2003) 1289-1319. https://doi.org/10.1016/S0143-974X(03)00067-1.
[53] L. DiSarno, A.S. Elnashai, D.A. Nethercot, Seismic response of stainless steel braced frames, Journal of Constructional Steel Research 64(7) (2008) 914-925. https://doi.org/10.1016/j.jcsr.2008.01.027.
[54] A.S. Tzimas, G.S. Kamaris, T.L. Karavasilis, C. Galasso, Collapse risk and residual drift performance of steel buildings using post-tensioned MRFs and viscous dampers in near-fault regions, Bulletin of Earthquake Engineering 14(6) (2016) 1643-1662. https://doi.org/10.1007/s10518-016-9898-3.
[55] Eurocode, Eurocode 3: Design of steel structures. 1-1: General rules and rules for buildings. EN 1993-1-1, 3 ed., European Standard (CEN), Brussels, Belgium, 2005.
[56] Eurocode, Eurocode 8: Design of structures for earthquake resistance. 1: General rules, seismic action and rules for buildings. EN 1998-1-1, 8 ed., European Standard (CEN), Brussels, Belgium, 2005.
[57] EN, EN ISO 6892-1: Metallic Materials - Tensile testing — Part 1: Method of test at room temperature, ISO 6892-1 ed., European Standard (CEN), Brussels, Belgium, 2009.
[58] I. Arrayago, E. Real, L. Gardner, Description of stress–strain curves for stainless steel alloys, Materials & Design 87 (2015) 540-552. https://doi.org/10.1016/j.matdes.2015.08.001.
[59] A.I.o.S. Construction, American Institute of Steel Construction (AISC). Seismic provisions for structural steel buildings, AISC, Chicago, 2005.
[60] Abaqus, Abaqus. Abaqus Documentation, Dassault Systèmes, Providence, RI, USA, 2022.
[61] M. Gkantou, M. Bock, M. Theofanous, Design of stainless steel cross-sections with outstand elements under stress gradients, J. Constr. Steel Res. 179 (2021) 106491. https://doi.org/10.1016/j.jcsr.2020.106491.
[62] R. Nascimbene, Penalty partial reduced selective integration: a new method to solve locking phenomena in thin shell steel and concrete structures, Curved and Layered Structures 9(1) (2022) 352-364. doi:10.1515/cls-2022-

0027.

[63] H. Ban, J. Zhu, G. Shi, Cyclic loading tests on welded connections of stainless-clad bimetallic steel and modelling, Journal of Constructional Steel Research 171 (2020) 106140. https://doi.org/10.1016/j.jcsr.2020.106140.

[64] C. Couto, P. Vila Real, Numerical investigation on the influence of imperfections in the lateral-torsional buckling of beams with slender I-shaped welded sections, Thin-Walled Struct. 145 (2019) 106429. https://doi.org/10.1016/j.tws.2019.106429.

[65] H.X. Yuan, Y.Q. Wang, Y.J. Shi, L. Gardner, Residual stress distributions in welded stainless steel sections, Thin-Walled Struct. 79 (2014) 38-51. https://doi.org/10.1016/j.tws.2014.01.022.

[66] H. Fang, T.-M. Chan, Buckling resistance of welded high-strength-steel box-section members under combined compression and bending, J. Constr. Steel Res. 162 (2019) 105711. https://doi.org/10.1016/j.jcsr.2019.105711.